ADVANCED MATERIALS INTERFACES

www.advmatinterfaces.de

Crack Control in Biotemplated Gold Films for Wide-Range, Highly Sensitive Strain Sensing

Jidong Shi, Suye Lv, Liu Wang, Zhaohe Dai, Siting Yang, Lingyu Zhao, Huihui Tian, Mingde Du, Hongbian Li, and Ying Fang**

Strain sensors with high sensitivity and large sensing range have great potential in a wide range of applications. However, in the design of strain sensors, there is usually a trade-off between sensitivity and sensing range. Herein, a crack-based strain sensor with engineered microstructure is facilely prepared through a biotemplating method. Under large tensile strains, randomly distributed microcavities on the strain sensor surface can effectively trap and terminate propagating cracks to prevent catastrophic fracture failure. As a result, the strain sensor shows both wide sensing range (up to 80%) and high sensitivity (gauge factor = 20 at 20% strain, 350 at 80% strain). The strain sensor enables sensitive and reliable detection of both subtle human motions, including wrist pulse and throat vibration, and large motions, such as finger bending. Moreover, a multipixel strain sensor array has been fabricated and applied for both static and dynamic strain mapping. The good sensing performance, together with its easy-fabrication process, make the biotemplated strain sensor a promising candidate for applications in e-skins and wearable electronics.

1. Introduction

Flexible and wearable strain sensors have been attracting great interests in recent years for applications in health monitoring, human motion detection, and human–machine interfaces.[1–7] Over the past few years, significant advances have been made in the development of flexible strain sensors based on different sensing mechanisms.[8–10] In particular, resistive strain sensors have been widely explored due to their simple structure and easy read-out systems.[11] Resistive strain sensors are typically constructed by the integration of an electrically functional component and a stretchable elastomer substrate. The performance of the strain sensors is typically evaluated by both the sensitivity (gauge factor = $(\Delta R/R_0)/\varepsilon$, where R_0 is the original electrical resistance of the strain sensor, ΔR is the change of electrical resistance upon strain, ε is the strain value) and the sensing range (maximum tolerable strain). However, high sensitivity and wide sensing range are usually trade-off properties in resistive strain sensors. For example, resistive strain sensors based on random or aligned networks of 1D nanostructures, such as carbon nanotubes and silver (Ag) nanowires, are particularly suitable to monitor large strains, such as finger-bending and walking.[12–17] The sliding and rotating of nanotubes or nanowires allow their networks to maintain electrical integrity up to 280% tensile strain,[16] leading to a large sensing range (Table S1, Supporting Information).[12–15] Under small strains, however, there are minimal changes in the conducting pathways within the networks. As a result, the sensitivity of these strain sensors is usually low (GF < 5 at a strain of 20%), which limits their applications in the detection of subtle deformations, such as pulse and throat vibrations.[12–14,16,17] On the other hand, resistive strain sensors based on silicon or metal thin films have shown extremely high sensitivity by generating cracks in the brittle films.[18–21] For example, Kang et al. developed a crack-based strain sensor using thin platinum films and achieved a gauge factor of over 2000 at strains of 0%–2% (Table S1, Supporting Information).[19] However, under large strains, the rapid propagation of cracks caused catastrophic fracture of the metal films and thus led to open circuits. As a result, the sensing range of previous strain sensors based on cracked brittle thin films have been quite limited (<2%),[19–21] which is well below the requirement for full-range human motion detection (over 55%).[16]

The fracture failure limit of brittle thin films strongly depends on their crack propagation behaviors.[22–25] In previous

Dr. J. Shi, S. Lv, S. Yang, Dr. L. Zhao, Dr. H. Tian, Dr. M. Du, Prof. H. Li, Prof. Y. Fang
CAS Key Laboratory for Biomedical Effects of Nanomaterials and Nanosafety
CAS Center for Excellence in Nanoscience
National Center for Nanoscience and Technology
Beijing 100190, China
E-mail: lihb@nanoctr.cn; fangy@nanoctr.cn

Dr. J. Shi, S. Lv, S. Yang, Dr. L. Zhao, Dr. M. Du
University of Chinese Academy of Sciences
Beijing 100049, China

Dr. L. Wang, Z. Dai
Center for Mechanics of Solids, Structures and Materials
Department of Aerospace Engineering and Engineering Mechanics
The University of Texas at Austin
Austin, TX 78712, USA

Prof. Y. Fang
CAS Center for Excellence in Brain Science and Intelligence Technology
320 Yue Yang Road, Shanghai 200031, China

The ORCID identification number(s) for the author(s) of this article can be found under https://doi.org/10.1002/admi.201901223.

DOI: 10.1002/admi.201901223

crack-based strain sensors, catastrophic breakage of the thin metal films was triggered by the rapid propagation of cracks beyond a critical length.[19,20] Thus, it is necessary to control crack growth at the microscopic level in order to obtain a wide sensing range. Recent studies show that the crack growth patterns in thin metal films can be controlled by engineering metal–polymer interfaces. For example, Chen and co-workers found that crack propagation can be effectively suppressed by interlocking an Au film with the underlying poly(dimethylsiloxane) (PDMS) substrate, and the stretchability of the Au film was increased to 40% (Table S1, Supporting Information).[22] Lee et al. developed a mogul-patterned stretchable substrate using double photolithography, and the stretchability of the Au film on the mogul-patterned substrate reached 50% (Table S1, Supporting Information).[23] The improved stretchability of these Au films can be attributed to the introduction of local stress inhomogeneity, which effectively modifies the generation and propagation behavior of cracks under tensile strains. Nevertheless, the Au films in previous studies have low strain sensitivity (GF < 14 at a strain of 50%) (Table S1, Supporting Information),[23] and the patterning processes of the microstructured metal–polymer interfaces were relatively complicated. Thus, it is highly desirable to develop a simple and scalable approach for the fabrication of crack-based strain sensors that can provide both high sensitivity and large sensing range.

Herein, we develop a simple and scalable biotemplating method to introduce microcavities in an Au thin film-based strain sensor. The microcavities efficiently increase the interfacial adhesion between the metal thin film and the elastomer substrate of the sensor. Moreover, the microcavities can effectively control crack growth patterns in the strain sensor by trapping and terminating propagating cracks, which prevents catastrophic fracture failure up to a tensile strain of ≈90%. As a result, the strain sensor shows both high sensitivity (gauge factor = 20 at 20% strain, 350 at 80% strain) and wide sensing range (≈80%). The easy preparation and good performance of the biotemplated strain sensor make it a promising candidate for applications in e-skins and wearable electronics.

2. Results and Discussions

A patterned PDMS was fabricated by a one-step molding process with a lotus leaf as the template. As shown in **Figure 1**a, a mixture of PDMS precursor and curing agent, at a ratio of 10:1, was poured onto the surface of the lotus leaf. After curing at 60 °C for 2 h, the lotus leaf could be readily peeled off, and a negative PDMS replica was obtained. Then an 80-nm-thick Au film was sputtered onto the surface of the negative PDMS replica, resulting in an engineered Au/PDMS (*e*-Au/PDMS) film that is highly flexible, stretchable, and twistable (Figure 1b).

The surface of the lotus leaf consists of numerous microscale papillae with an average height of 5–9 µm, and the surface of the micropapillae is covered with nanofibers of 100–200 nm in diameter and ≈500 nm in length (Figure S1, Supporting Information).[26] As a result, the surface of the *e*-Au/PDMS is patterned with randomly distributed microscale cavities (Figure 1c). The microcavities have an inverted cone structure, which facilitates the uniform deposition of Au both inside and outside the microcavities to form a continuous metal film (Figure 1d). In addition, the microcavities are decorated with nanowrinkles, leading to a hierarchical surface structure. We note the surface roughness of the *e*-Au/PDMS was lower than that of the lotus leaf, which could be attributed to an incomplete surface wetting of the PDMS precursor during the biotemplating process. From the cross-sectional image of the *e*-Au/PDMS film in Figure 1e and the 3D confocal image in Figure 1f, the depth of the microcavities was measured to be 5–6.5 µm, which is slightly smaller than the average height of the micropapillae on the lotus leaf. This can be explained by the

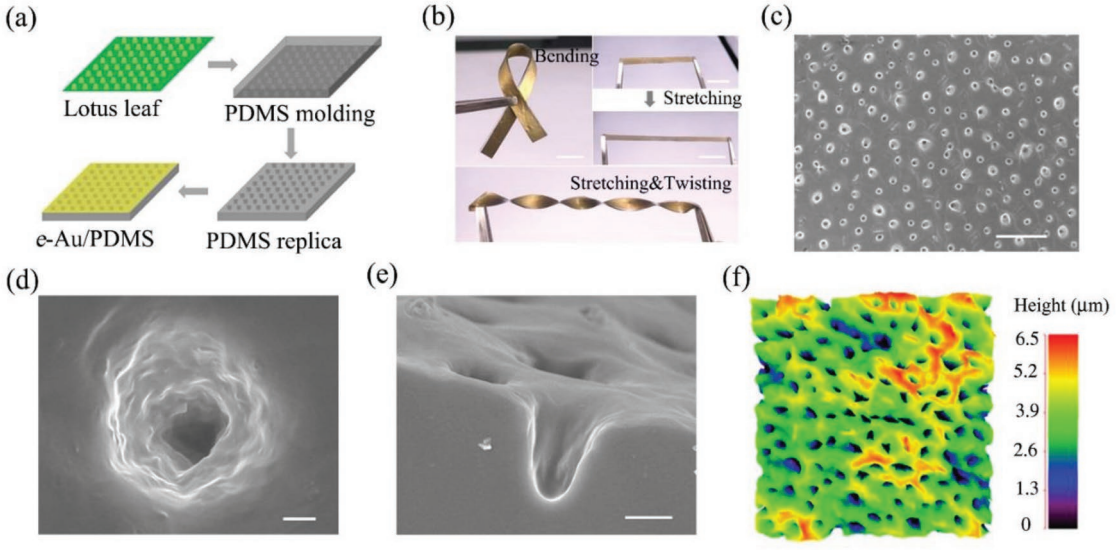

Figure 1. Preparation and morphological characterizations of *e*-Au/PDMS films. a) Schematic illustration of the preparation process of an *e*-Au/PDMS film. b) Photograph of an *e*-Au/PDMS film during bending, stretching, and stretching and twisting. Scale bars: 1 cm. c) SEM image of an *e*-Au/PDMS film. Scale bar: 50 µm. d) Magnified SEM view of a microcavity with nanowrinkles. Scale bar: 2 µm. e) Cross-sectional image of an *e*-Au/PDMS film. Scale bar: 5 µm. f) 3D confocal image of the *e*-Au/PDMS film.

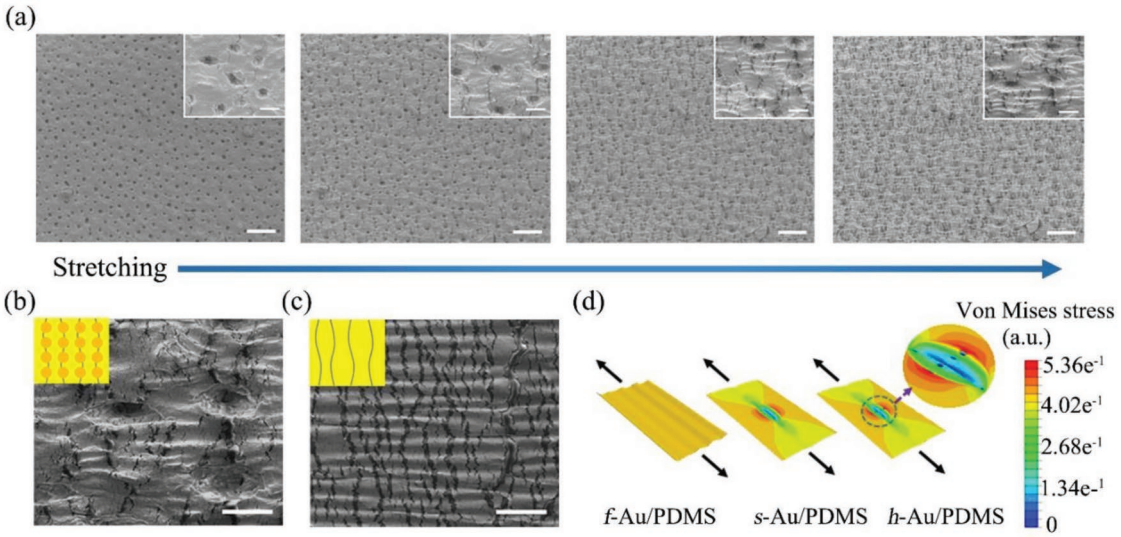

Figure 2. Morphological characterizations of Au/PDMS films under tensile strains. a) Morphological evolution of an *e*-Au/PDMS film at tensile strains from 0 to 20%, 40%, and 60%. Scale bars: 50 µm. Inset images are the magnified view of the cracks in the Au film. Inset scale bars: 10 µm. b) Magnified view of an *e*-Au/PDMS film under 40% tensile strain. Inset, schematic illustration of the crack pattern in the *e*-Au/PDMS film. Scale bar: 10 µm. c) Magnified view of an *f*-Au/PDMS film under 40% tensile strain. Inset, schematic illustration of the crack pattern in the *f*-Au/PDMS film. Scale bar: 10 µm. d) FEA analysis of strain distribution in stretched *f*-Au/PDMS, *s*-Au/PDMS, and *h*-Au/PDMS films.

volume shrinkage of the PDMS replica to release the compressive stress from polymerization.

We first investigated the morphological changes of the *e*-Au/PDMS films under tensile strains. As shown in **Figure 2**a, the application of a tensile strain induces cracks in the Au film of an *e*-Au/PDMS film, and the areal density of the cracks increases with the tensile strain. Importantly, the cracks are mainly localized between adjacent microcavities, and no long cracks were observed in the metal film even at a strain of 60%. Figure 2b,c shows the magnified images of cracks on an *e*-Au/PDMS and a flat Au/PDMS (*f*-Au/PDMS), respectively, under a tensile strain of 40%. For the *e*-Au/PDMS, most cracks in the metal film are trapped and terminated at the edge of the microcavities, which dramatically decreases the average length and width of the cracks (Figure 2b). By contrast, the cracks on the *f*-Au/PDMS rapidly propagate in the direction perpendicular to the stretching direction (Figure S2, Supporting Information).[27,28] Under 40% strain, long and wide cracks result in the complete breakage of the Au film in the *f*-Au/PDMS (Figure 2c).

In order to understand the mechanism for the formation of different crack morphologies in *e*-Au/PDMS and *f*-Au/PDMS, we carried out finite element analysis (FEA) to simulate the strain distribution in the Au films under the same tensile strain (48%). Three types of Au/PDMS structures are modeled: *f*-Au/PDMS (Figure S3a, Supporting Information), Au/PDMS with smooth hemisphere microcavities (*s*-Au/PDMS, Figure S3b, Supporting Information), and Au/PDMS with hierarchical microcavities (*h*-Au/PDMS, Figure S3c, Supporting Information). For the stretched *f*-Au/PDMS, the strain distribution is relatively uniform across the Au film, and transverse wave-like wrinkles are formed in the Au film due to the Poisson's effect (Figure 2d, left; Figure S3d, Supporting Information). As a result, cracks in the flat Au film will propagate along straight path.[29] On the other hand, the strain distribution in the stretched *s*-Au/PDMS is dramatically altered by the microcavities.[30,31] The stress concentration is the highest at the edges of the microcavities (Figure 2d, middle; Figure S3e, Supporting Information), whereas the inside surface of the microcavities has the lowest stress concentration. It is known that brittle cracks propagate along the path where the highest stresses are accumulated.[20] Thus, the high stress concentration of the microcavities can effectively trap the cracks, whereas the low stress concentration inside the microcavities terminate the propagation of the cracks.[25] The introduction of second-order cavities on the surface of first-order cavities in the *h*-Au/PDMS leads to additional stress inhomogeneity inside the cavities (Figure 2d, right; Figure S3f, Supporting Information). Moreover, the hierarchical surface in the *h*-Au/PDMS can increase the effective contact area between the Au and the PDMS, enhancing the interfacial adhesion thus further reducing the propagation rate of cracks.[23,24,32] From the results above, it can be seen that the hierarchical surface of our biotemplated *e*-Au/PDMS can effectively control crack growth and maintain the electrical integrity of the Au film under large tensile strains.

Next, we characterized the electromechanical response of the *e*-Au/PDMS films under continuously increased tensile strains, and representative results are summarized in **Figure 3**a,b, and Figure S5 (Supporting Information). During initial loading, the resistance of an *e*-Au/PDMS film increased exponentially with the tensile strain because of the initialization and fast growth of cracks in the Au film. Significantly, the *e*-Au/PDMS film maintained its electrical integrity even at a strain as high as 90%. By contrast, the *f*-Au/PDMS film lost its electrical conductivity above a tensile strain of 12.5% because of the formation of penetrating cracks (Figure 3b). We further fabricated a Scindapsus auteus (SA) leaf-patterned Au/PDMS film and studied its electromechanical response under different tensile strains. The surface of the SA leaf-patterned Au/PDMS film

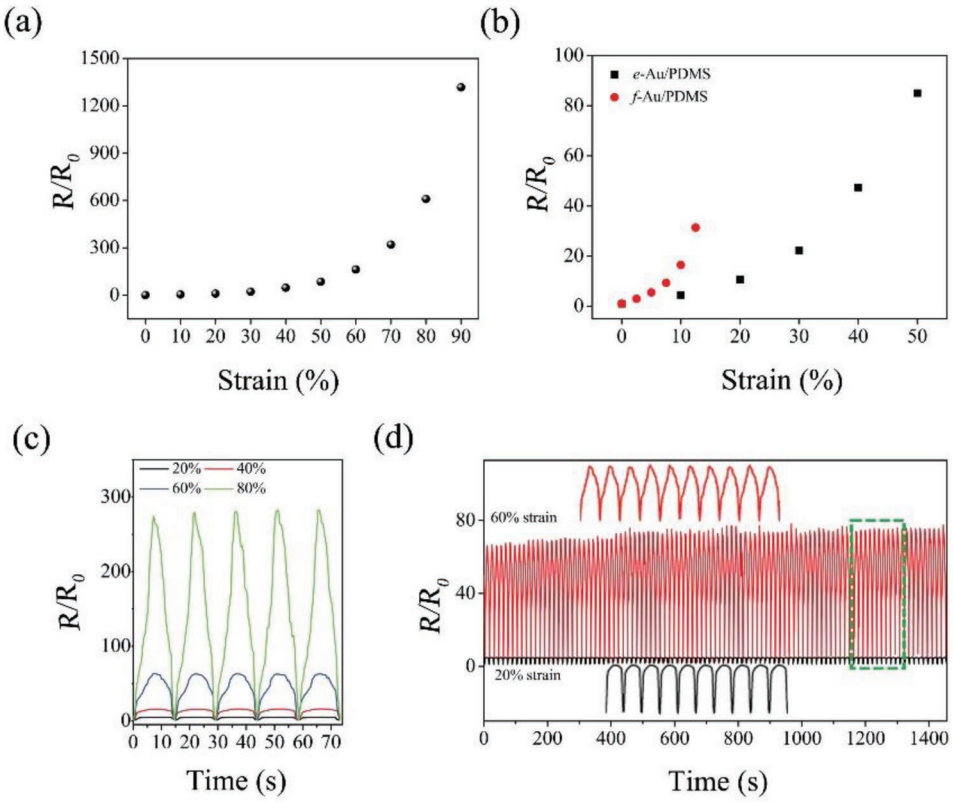

Figure 3. Electromechanical behaviors of *e*-Au/PDMS films. a) Resistive response of an *e*-Au/PDMS film under a monotonic increased tensile strain from 0% to 90%. b) Comparison of the electromechanical responses between an *e*-Au/PDMS film and an *f*-Au/PDMS film. c) Resistive response of an *e*-Au/PDMS film under 20%, 40%, 60%, and 80% tensile strains. d) Stability test (100 cycles) of an *e*-Au/PDMS film under 20% (black) and 60% (red) tensile strains, respectively. Inset, magnified view of the green dashed box.

consists of distributed microdomes of 65 μm in length and 3 μm in height.[33] As shown in Figure S4 (Supporting Information), the SA leaf-patterned Au/PDMS film lost its electrical conductivity above a tensile strain of 30%. Therefore, although the smooth and shallow microdomes can enhance the stretchability of the Au/PDMS films to some extent, they are not as effective as the hierarchical microcavities in lotus leaf-patterned Au/PDMS films. In addition, the thickness of the Au layer also plays an important role in determining the stretchability of the *e*-Au/PDMS film. The maximum operational strains for the 40 and 120-nm-thick Au film were 50% and 80%, respectively (Figure S6, Supporting Information).

The high stretchability and sensitive electromechanical response make the *e*-Au/PDMS films an attractive candidate for use in strain sensors. As shown in Figure 3c, an *e*-Au/PDMS strain sensor shows reliable resistive response up to 80% tensile strain. The gauge factors were determined to be 20 for 20% and 350 for 80% tensile strains, respectively. Moreover, the good stability of the strain sensor was confirmed by performing 100 cyclic loadings in both low (20%) and high (60%) strain ranges (Figure 3d). The slight increase in the resistance response of the sensor at the beginning of the cycling test might be due to the emergence and propagation of cracks.

We have compared our results with previous studies in Table S1 in the Supporting Information. Our *e*-Au/PDMS strain films offer both high sensitivity and large sensing range and thus can be utilized for sensitive detection of both subtle and large strains. As a demonstration, an *e*-Au/PDMS strain sensor was attached onto a human wrist for real-time monitoring of the subtle pulse signal.[34,35] As shown in **Figure 4**a,b, the percussion waves (P1) and tidal waves (P2) can be clearly identified in the recorded pulse signal, and the corresponding heart rate was determined to be 81 beats per min.[36] Moreover, the *e*-Au/PDMS strain sensor could also be attached onto a human throat to monitor minute vibrations of swallowing, breathing, and speaking (Figure S7, Supporting Information).[37] In addition, the strain sensor could distinguish different words played by a loudspeaker (Figure S8, Supporting Information). We further applied the *e*-Au/PDMS films for the detection of large strains. As shown in Figure 4c, an *e*-Au/PDMS strain sensor was mounted onto the proximal interphalangeal (PIP) joint of the index finger, and the resistive response of the strain sensor increased with the bending angle of the finger. The above results demonstrate that our *e*-Au/PDMS strain sensor can be applied for human health monitoring and human motion detection.

In many practical applications, it is highly desirable to integrate multiple sensors in a device array for spatially resolved strain measurements.[38] As a proof of concept, we constructed a flexible 4 × 5 pixel array of the biotemplated strain sensors (Figure 4d). Each pixel has a dogbone shape, consisting of a 3 × 1 mm channel and two 2 mm × 2 mm pads. The

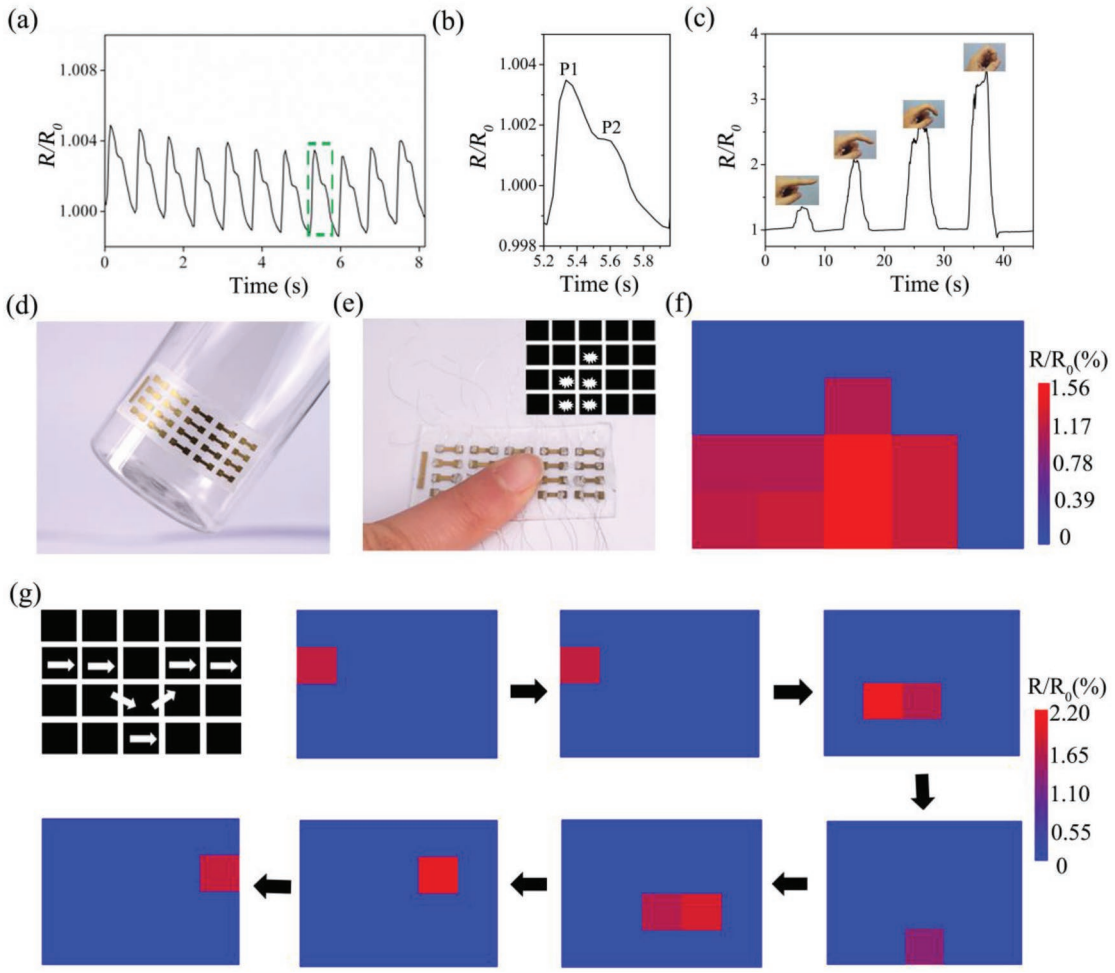

Figure 4. Applications of *e*-Au/PDMS strain sensors for human motion detection and strain mapping. a) Relative resistance-time curve of an *e*-Au/PDMS in response to pulse vibration. Inset, optical image of the device attached on a human wrist. b) Magnified view of the single pulse waveform in the green dashed box in inset (a). c) Relative resistance-time curve of an *e*-Au/PDMS in response to finger bending at different angles. d) Optical image of a flexible strain sensor array conformally attached onto a cylindrical bottle. e) Optical image of a strain sensor array compressed by a finger. Inset, schematic of the devices underneath the finger. f) Resistive response of the strain sensor array to finger compressing as in inset (e). g) Time-series resistive response of the strain sensor array to dynamic strain loads.

center-to-center distance between adjacent pixels is 7 mm. As shown in Figure 4e,f, the resistive outputs of the sensing array corresponded well with the position of the finger. Moreover, the device array could also be applied for real-time strain mapping. Figure 4g shows the time-series response of the array when a tweezer passed through the devices along the marked trajectory. The spatial resolved strain detection by the multipixel sensor array makes it a promising candidate for the development of integrated e-skins.

3. Conclusion

In summary, we have developed a crack-based *e*-Au/PDMS strain sensor through surface microstructure engineering. The hierarchical microscale cavities and nanoscale roughness in the engineered strain sensor surface effectively inhibit the propagation of catastrophic cracks at large tensile strains. Therefore, both high sensitivity (20 at 20% strain to 350 at 80% strain) and wide sensing range (80%) have been simultaneously achieved in the *e*-Au/PDMS strain sensor. The sensor has been successfully demonstrated in the detection of subtle strains, including pulse, throat vibrations, and sound vibrations, as well as large strains, such as finger bending. Moreover, spatial resolved detection of both static and dynamic strain has been achieved by a multipixel strain sensor array. The combined advantages of high sensitivity and wide sensing range, together with its simple and large-scale fabrication process, make our strain sensor a promising candidate for e-skins and wearable electronics.

4. Experimental Section

Preparation of the e-Au/PDMS Films: Lotus leaves were collected from the campus lake of Beihang University. After cleaning, a lotus leaf was cut into pieces and taped onto a glass petri dish. Then a mixture of PDMS precursor and curing agent at a ratio of 10:1 (by weight, Dow Corning) was poured onto the surface of the lotus leaf. After curing at

60 °C for 2 h, the lotus leaf was peeled off and a negative PDMS replica was obtained. The patterned PDMS was put into a sputter to deposit Au to obtain an *e*-Au/PDMS film. Then, the Au film was connected to two Ag wires using liquid metal (gallium–indium eutectic) droplets for resistance measurements.

Structure Characterizations: Surface morphologies of specimens were characterized by a scanning electron microscope (SEM, Nova 430) and a confocal microscopy (Olympus, LEXT OLS4100). To characterize the cross-section, a negative PDMS replica was cut with a sharp razor blade, and then 30-nm-thick Au was sputtered onto the PDMS before SEM analysis.

Strain Sensing Tests: Mechanical strains were applied by a dynamic mechanical analyzer (DMA) manufactured by TA instrument company, and the resistance was recorded in situ by a Keithley 4200-SCS semiconductor parameter analyzer.

FEA Simulation: FEA was conducted using commercial package ABAQUS/Standard 6.13. The 80-nm-thick gold film was modeled as an elastic shell while the thick PDMS substrate was modeled as an incompressible neo-Hookean material. Periodic microscale cavities were modeled in the *s*-Au/PDMS (Figure S3b, Supporting Information). A square-patterned array of hemisphere cavities was assumed, with diameter and centre-to-centre spacing equal to 5 and 20 μm, respectively. Considering the periodicity of the square-patterned array, a unit cell with width = length = 20 μm suffices for the simulation where periodic boundary conditions are applied. The applied tensile strain was 48%. To elucidate the effect of the surface structure on the strain distribution in the Au film, 13 spherical domes (diameter: 0.5 μm) were added on the surface of the microscale hemisphere for *h*-Au/PDMS (Figure S3c, Supporting Information). These domes were uniformly distributed in two orthogonal directions, i.e., perpendicular and parallel to the loading direction.

Supporting Information

Supporting Information is available from the Wiley Online Library or from the author.

Acknowledgements

Y.F. thanks the support from National Natural Science Foundation of China (21790393), and CAS Key Research Program of Frontier Sciences (XDB32030100).

Conflict of Interest

The authors declare no conflict of interest.

Keywords

crack control, health monitoring, metal thin films, microstructure engineering, strain sensors

Received: July 16, 2019
Revised: August 9, 2019
Published online: September 8, 2019

[1] M. Amjadi, K. U. Kyung, I. Park, M. Sitti, *Adv. Funct. Mater.* **2016**, *26*, 1678.
[2] S. W. Ryu, P. Lee, J. B. Chou, R. Z. Xu, R. Zhao, A. J. Hart, S. G. Kim, *ACS Nano* **2015**, *9*, 5929.
[3] E. Roh, B. U. Hwang, D. Kim, B. Y. Kim, N. E. Lee, *ACS Nano* **2015**, *9*, 6252.
[4] Z. H. Huo, Y. Y. Peng, Y. F. Zhang, G. Y. Gao, B. S. Wan, W. Q. Wu, Z. Yang, X. D. Wang, C. F. Pan, *Adv. Mater. Interfaces* **2018**, *5*, 1801061.
[5] N. S. Liu, G. J. Fang, J. W. Wan, H. Zhou, H. Long, X. Z. Zhao, *J. Mater. Chem.* **2011**, *21*, 18962.
[6] W. J. Liu, N. S. Liu, Y. Yue, J. Y. Rao, F. Cheng, J. Su, Z. T. Liu, Y. H. Gao, *Small* **2018**, *14*, 1704149.
[7] Y. Yue, N. S. Liu, W. J. Liu, M. Li, Y. N. Ma, C. Luo, S. L. Wang, J. Y. Rao, X. K. Hu, J. Su, Z. Zhang, Q. Huang, Y. H. Gao, *Nano Energy* **2018**, *50*, 79.
[8] A. Frutiger, J. T. Muth, D. M. Vogt, Y. Mengüc, A. Campo, A. D. Valentine, C. J. Walsh, J. A. Lewis, *Adv. Mater.* **2015**, *27*, 2440.
[9] J. W. Zhong, Y. Zhang, Q. Z. Zhong, B. Hu, Z. L. Wang, J. Zhou, *ACS Nano* **2014**, *8*, 6273.
[10] X. M. Li, T. T. Yang, Y. Yang, J. Zhu, L. Li, F. E. Alam, X. Li, K. L. Wang, H. Y. Cheng, C.-T. Lin, Y. Fang, H. W. Zhu, *Adv. Funct. Mater.* **2016**, *26*, 1322.
[11] N. N. Jason, M. D. Ho, W. L. Cheng, *J. Mater. Chem. C* **2017**, *5*, 5845.
[12] L. Cai, J. Z. Li, P. S. Luan, H. B. Dong, D. Zhao, Q. Zhang, X. Zhang, M. Tu, Q. S. Zeng, W. Y. Zhou, S. S. Xie, *Adv. Funct. Mater.* **2012**, *22*, 5238.
[13] M. Amjadi, A. Pichitpajongkit, S. J. Lee, S. Ryu, I. Park, *ACS Nano* **2014**, *8*, 5154.
[14] J. D. Shi, X. M. Li, H. Y. Cheng, Z. J. Liu, L. Y Zhao, T. T. Yang, Z. H. Dai, Z. G. Cheng, E. Z. Shi, L. Yang, Z. Zhang, A. Y. Cao, H. W. Zhu, Y. Fang, *Adv. Funct. Mater.* **2016**, *26*, 2078.
[15] J. D. Shi, J. Hu, Z. H. Dai, W. Zhao, P. Liu, L. Y. Zhao, Y. C. Guo, T. T. Yang, L. Zou, K. L. Jiang, H. B. Li, Y. Fang, *Carbon* **2017**, *123*, 786.
[16] T. Yamada, Y. H. Hayamizu, Y. Yamamoto, Y. Yomogida, A. Izadi-Najafabadi, D. N. Futaba, K. Hata, *Nat. Nanotechnol.* **2011**, *6*, 296.
[17] H. F. Zhu, X. W. Wang, J. Liang, H. L. Lv, H. Y. Tong, L. B. Ma, Y. Hu, G. Y. Zhu, T. Zhang, Z. X. Tie, Z. Liu, Q. W. Li, L. W. Chen, J. Liu, Z. Jin, *Adv. Funct. Mater.* **2017**, *27*, 1606604.
[18] Y. Kervran, O. D. Sagazan, S. Crand, N. Coulon, T. Mohammed-Brahim, O. Brel, *Sens. Actuators, A* **2015**, *236*, 273.
[19] D. Kang, P. V. Pikhitsa, Y. W. Choi, C. Lee, S. S. Shin, L. F. Piao, B. Park, K. Y. Suh, T. Kim, M. Choi, *Nature* **2014**, *516*, 222.
[20] T. T. Yang, X. M. Li, X. Jiang, S. Y. Lin, J. C. Lao, J. D. Shi, Z. Zhen, Z. H. Li, H. W. Zhu, *Mater. Horiz.* **2016**, *3*, 248.
[21] J. L. Ye, T. T. Yang, Y. F. Zhang, L. Lin, *Adv. Mater. Interfaces* **2018**, *5*, 1800616.
[22] Z. Y. Liu, X. T. Wang, D. P. Qi, C. Xu, J. C. Yu, Y. Q. Liu, Y. Jiang, B. Liedberg, X. D. Chen, *Adv. Mater.* **2017**, *29*, 1603382.
[23] H. B. Lee, C. W. Bae, L. T. Duy, I. Y. Sohn, D. I. Kim, Y. J. Song, Y. J. Kim, N. E. Lee, *Adv. Mater.* **2016**, *28*, 3069.
[24] B. Zhang, J. Lei, D. P. Qi, Z. Y. Liu, Y. Wang, G. W. Xiao, J. S. Wu, W. N. Zhang, F. W. Huo, X. D. Chen, *Adv. Funct. Mater.* **2018**, *28*, 1801683.
[25] R. S. Guo, Y. Yu, J. F. Zeng, X. Q. Liu, X. C. Zhou, L. Y. Niu, T. T. Gao, K. Li, Y. Yang, F. Zhou, Z. J. Zheng, *Adv. Sci.* **2015**, *2*, 1400021.
[26] W. Barthlott, C. Neinhuis, *Planta* **1997**, *202*, 1.
[27] I. M. Graz, D. P. J. Cotton, S. P. Lacour, *Appl. Phys. Lett.* **2009**, *94*, 071902.
[28] N. S. Lu, X. Wang, Z. G. Suo, J. Vlassak, *Appl. Phys. Lett.* **2007**, *91*, 221909.
[29] Y. Xiang, T. Li, Z. G. Suo, J. J. Vlassak, *Appl. Phys. Lett.* **2005**, *87*, 161910.
[30] T. Li, Z. Y. Huang, Z. C. Xi, S. P. Lacour, S. Wagner, Z. G. Suo, *Mech. Mater.* **2005**, *37*, 261.
[31] S. H. Peng, P. Blanloeuil, S. Y. Wu, C. H. Wang, *Adv. Mater. Interfaces* **2018**, *5*, 1800403.

[32] Y. Yu, C. Yan, Z. J. Zheng, *Adv. Mater.* **2014**, *26*, 5508.
[33] M. Q. Jian, K. L. Xia, Q. Wang, Z. Yin, H. M. Wang, C. Y. Wang, H. H. Xie, M. C. Zhang, Y. Y. Zhang, *Adv. Funct. Mater.* **2017**, *27*, 1606066.
[34] Q. Wang, M. Q. Jian, C. Y. Wang, Y. Y. Zhang, *Adv. Funct. Mater.* **2017**, *27*, 1605657.
[35] J. D. Shi, L. Wang, Z. H. Dai, L. Y. Zhao, M. D. Du, H. B. Li, Y. Fang, *Small* **2018**, *14*, 1800819.
[36] T. T. Yang, W. Wang, H. Z. Zhang, X. M. Li, J. D. Shi, Y. J. He, Q. S. Zheng, Z. H. Li, H. W. Zhu, *ACS Nano* **2015**, *9*, 10867.
[37] Y. C. Wu, I. Karakurt, L. Beker, Y. Kubota, R. X. Xu, K. Y. Ho, S. L. Zhao, J. W. Zhong, M. Zhang, X. H. Wang, L. W. Lin, *Sens. Actuators, A* **2018**, *279*, 46.
[38] W. Feng, W. Zheng, F. Gao, X. S. Chen, G. B. Liu, T. Hasan, W. W. Cao, P. A. Hu, *Chem. Mater.* **2016**, *28*, 4278.

